J Biomol NMR (2012) 54:1–7
DOI 10.1007/s10858-012-9646-1

COMMUNICATION

# Parallel acquisition of multi-dimensional spectra in protein NMR

**Ēriks Kupče · Lewis E. Kay**

Received: 30 April 2012 / Accepted: 15 June 2012 / Published online: 17 July 2012


**Abstract** We introduce the use of multiple receivers applied in parallel for simultaneously recording multi-dimensional data sets of proteins in a single experiment. The utility of the approach is established through the introduction of the 2D $^{15}$N,$^{1}$H$^{N}$‖$^{13}$CO HSQC experiment in which a pair of two-dimensional $^{15}$N,$^{1}$H$^{N}$ and $^{15}$N,$^{13}$CO spectra are recorded. The methodology is further extended to higher dimensionality via the 3D $^{1}$H$^{N}$‖$^{13}$CO HNCA in which a pair of data sets recording $^{13}$C$^{\alpha}$,$^{15}$N,$^{1}$H$^{N}$ and $^{13}$C$^{\alpha}$,$^{15}$N,$^{13}$CO chemical shifts are acquired. With the anticipated increases in probe sensitivity it is expected that multiple receiver experiments will become an important approach for efficient recording of NMR data.

**Keywords** Multiple receivers · Protein NMR · Parallel acquisition · Multi-dimensional NMR · HSQC · HNCA

## Introduction

NMR spectroscopy has evolved into a powerful analytical tool for studies of complex molecules such as proteins (Bax 1994; Wüthrich 1986). Typically, resonance assignments are initially obtained, involving recording and analyzing a series of multi-dimensional spectra where different sets of nuclei are correlated in each data set (Clore and Gronenborn 1991; Ikura et al. 1990). These correlations are achieved using pulse schemes whereby chemical shifts are measured in a set of indirect detection periods, followed by direct detection of magnetization, most often proton, at the end of the experiment. The development of cryogenically cooled probes offering significant increases in sensitivity, along with the advent of multiple receivers provides the exciting possibility of changing this paradigm to better optimize the efficiency of spectrometer use. In principle, this can be realized because the use of parallel receivers facilitates the recording of multiple data sets from a single pulse scheme whereby both $^{13}$C and $^{1}$H nuclei are detected directly (Kupce 2011).

There are two main approaches for recording free induction decays (FIDs) in multi-receiver experiments and these involve either parallel or sequential acquisition. Both approaches typically split the magnetization into different pathways that are manipulated separately, with the resultant signals from each of the paths recorded using different receivers. The sequential acquisition method has been exploited in a number of applications to date involving a range of different molecules (Kupce and Freeman 2008; 2011; Kupce et al. 2006), including a scheme for recording simultaneous 2D HACACO and 3D HACACONNH spectra (Kupce et al. 2010) and more recently an experiment for obtaining $^{13}$C$^{\alpha}$–$^{15}$N and $^{1}$H–$^{15}$N–$^{15}$N sequential correlations in proteins (Chakraborty et al. 2012). Using the sequential approach it becomes possible, in some applications, to record signal from one pathway in parallel with an evolution step that is required of magnetization associated with the second pathway, leading to increased

Ē. Kupče
Agilent Technologies, 6 Mead Road, Yarnton, Oxford OX5 1QU, UK

L. E. Kay (✉)
Departments of Molecular Genetics, Biochemistry and Chemistry, The University of Toronto, Toronto, ON M5S 1A8, Canada
e-mail: kay@pound.med.utoronto.ca

L. E. Kay
Program in Molecular Structure and Function, Hospital for Sick Children, 555 University Avenue, Toronto, ON M5G 1X8, Canada

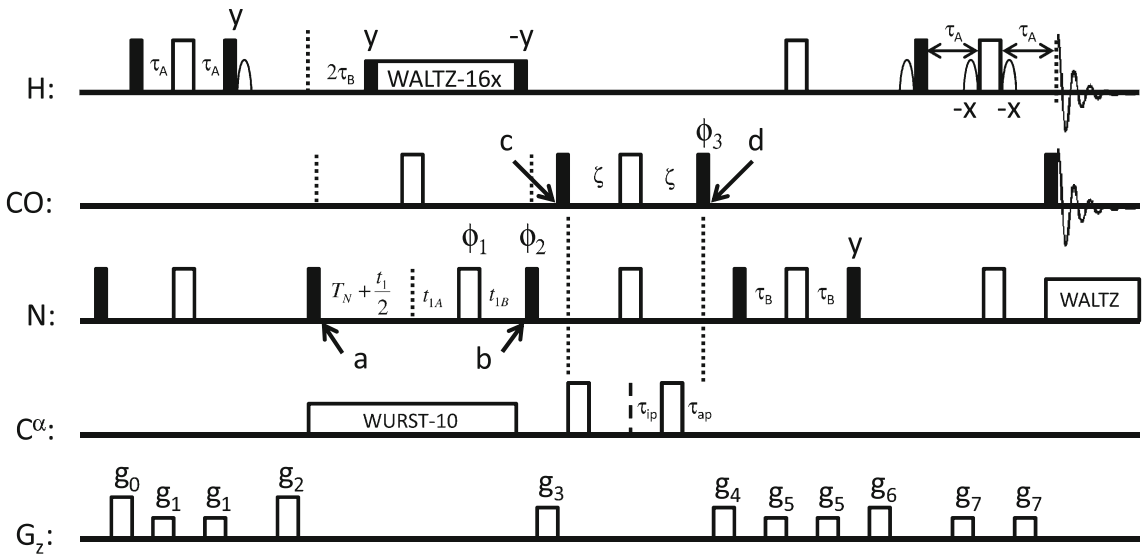


**Fig. 1** Pulse scheme for the 2D $^{15}$N,$^{1}$H$^{N}$‖$^{13}$CO HSQC experiment, with parallel acquisition of $^{1}$H$^{N}$ and $^{13}$CO signals during $t_2$. All filled (*open*) *rectangular* pulses have tip angles of 90° (180°), while shaped $^{1}$H pulses are water selective. The $^{1}$H, $^{13}$C and $^{15}$N carrier frequencies are positioned at the water line, at 176 ppm and at 119 ppm, respectively. $^{13}$C$^{\alpha}$ and $^{13}$CO pulses are applied at field strengths of $\Delta/\sqrt{15}$ and $\Delta/\sqrt{3}$ for tip angles of 90 and 180°, respectively, where $\Delta$ is the distance in Hz between the centers of the $^{13}$C$^{\alpha}$ and $^{13}$CO spectra (Kay et al. 1990). A small angle phase shift is applied to the $^{13}$CO 180° pulse between points *c* and *d* to compensate for the differences in power used for this pulse and the flanking 90° pulses. $^{13}$C$^{\alpha}$ decoupling during $t_1$ was achieved using a constant adiabaticity WURST-10 decoupling scheme (Kupce and Freeman 1996) with a bandwidth of 20 ppm centered at 58 ppm (swept from 48 to 68 ppm). The $B_{1max}$ ($B_{1rms}$) of the decoupling field was 0.5 (0.42) kHz (at 200 MHz $^{13}$C frequency). Delays: $\tau_A = 2.5$ ms, $\tau_B = 2.75$ ms, $T_N = \sim 15$ ms, $\zeta = 12.4$ ms. The value of $T_N$ is adjusted for optimal sensitivity for the $^{13}$CO detected pathway while retaining sufficient signal to noise for $^{1}$H$^{N}$ detection; by contrast $\zeta$ is chosen for optimal sensitivity for the $^{15}$N,$^{13}$CO spectrum and has essentially no effect on the $^{15}$N,$^{1}$H$^{N}$ correlation map. $^{15}$N evolution times are set as follows: if $T_N \geq t_1/2$ then $t_{1A} = 0$ and $t_{1B} = T_N - t_1/2$, otherwise $t_{1A} = t_1/2 - T_N$ and $t_{1B} = pw_{CO}$, where $pw_{CO}$ is the $^{13}$CO 180° pulse width. The acquisition times for the directly detected free induction decays of $^{13}$CO and $^{1}$H$^{N}$ nuclei were set to 82 ms with 1,024 complex data points acquired on both receivers at a sampling rate of 80 μs per data point. Phase cycling: $\phi_1 = x, y, -x, -y$; rec (both $^{1}$H and $^{13}$CO) = $x, -x$. Quadrature detection in $F_1$ was achieved by States-TPPI of $\phi_2$ (set to y for $\cos(\omega_N t_1)$ component of the $^{15}$N–$^{1}$H$^{N}$ data set) (Marion et al. 1989). The IPAP scheme (Ottiger et al. 1998; Yang and Nagayama 1996) is implemented by setting $\phi_3 =$ y, $\tau_{ip} = \zeta$ and $\tau_{ap} = 0$ to record the in-phase component and $\phi_3 = -$x, $\tau_{ip} = \zeta - \tau_{ap}$ and $\tau_{ap} = 4.86$ ms to record the anti-phase component. This has no effect on the $^{1}$H$^{N}$ detected signal. Gradient strengths (G/cm) and durations (ms): g0 = (10, 0.5), *g*1 = (5, 0.5), *g*2 = (15, 1), *g*3 = (11, 1), *g*4 = (7, 0.8), *g*5 = (−3, 0.3), *g*6 = (5, 0.6), *g*7 = (24, 0.4)

efficiency (Kupce et al. 2006). Further, because signals are recorded sequentially it is straightforward to decouple the detected magnetization from its coupling partners, as has been done in previous applications (Kupce 2011). A significant drawback, however, is that the direct detection periods that are within the pulse scheme, rather than at the end, are naturally restricted in length, limiting the available resolution. In principle, this problem can be overcome by parallel acquisition of signal from distinct pathways in the final step of the experiment so long as the observed nuclei are not scalar coupled or co-evolve with only very small scalar couplings. In what follows we illustrate the use of parallel acquisition for recording simultaneous multi-dimensional data sets of $^{15}$N,$^{13}$C labelled proteins, with specific applications to HSQC and HNCA pulse sequences incorporating simultaneous (parallel) $^{1}$H$^{N}$ and $^{13}$CO detection.

By means of illustration consider the pulse scheme of Fig. 1 in which a pair of two-dimensional $^{15}$N–$^{1}$H$^{N}$ and $^{15}$N–$^{13}$CO correlation experiments are recorded, $^{15}$N,$^{1}$H$^{N}$‖$^{13}$CO HSQC. The two-bond scalar couplings between $^{1}$H$^{N}$ and $^{13}$CO nuclei are uniformly small, 4.4 ± 0.4 Hz (Yang et al. 1999), so that decoupling of these nuclei from each other is not essential, and separate data sets can be acquired in parallel. In what follows we briefly outline the pertinent magnetization transfer schemes, neglecting the effects of pulse imperfections and spin relaxation. Immediately after the first INEPT period magnetization of interest is given by $2H_ZN_Z$, where $A_j\, j \in \{X,Y,Z\}$ is the *j* component of A magnetization. During the subsequent period between points *a* and *b* nitrogen transverse magnetization evolves with respect to the one-bond $^{15}$N–$^{13}$CO and $^{15}$N–$^{1}$H$^{N}$ scalar couplings and chemical shift so that immediately after gradient g3 the relevant terms are

$$\cos(2\pi J_{NCO}T_N)\cos(\omega_N t_1)N_Z - \sin(2\pi J_{NCO}T_N)\sin(\omega_N t_1)2N_ZCO_Z. \quad (1)$$

Each of the two components, $N_Z$ and $2N_ZCO_Z$, subsequently traverse separate pathways en-route to detection. Note that $N_Z$ is not affected by the element between *c* and *d*

(except for inversion), while immediately following $d$ the remaining portion of the pulse sequence transfers the nitrogen magnetization back to $^{1}H^{N}$ for detection. This pathway generates the 2D $^{15}N$,$^{1}H^{N}$ data set. By contrast, $2N_ZCO_Z$ is manipulated by the scheme between $c$ and $d$, to ultimately generate a '$^{13}C^{\alpha}$ decoupled, $^{13}CO$ detected data set' as described below, and the resultant magnetization stored along the Z-axis until the final CO 90° pulse prior to detection. This pathway is responsible for the $^{15}N$,$^{13}CO$ spectrum. Following the magnetization pathway for $2N_ZCO_Z$ one obtains $2N_ZCO_Z \rightarrow CO_Z$ for $\phi 3 = y$, $\tau_{ip} = \zeta$, $\tau_{ap} = 0$ and $2N_ZCO_Z \rightarrow 2CO_ZC_Z^{\alpha}$ for $\phi 3 = x$, $\tau_{ip} = \zeta - \tau_{ap}$, $\tau_{ap} = \frac{1}{4J_{CO,C\alpha}}$ where $J_{CO,C\alpha}$ is the uniform one bond $^{13}CO$,$^{13}C^{\alpha}$ scalar coupling (52.5 ± 1.0 Hz; Yang et al. 1999). Immediately after the final $^{13}CO$ pulse prior to detection the signal of interest is either $CO_Y$ (IP) or $2CO_YC_Z^{\alpha}$ (AP). The $^{15}N$,$^{13}CO$ data sets recorded as in-phase ($CO_Y$) or anti-phase ($2CO_YC_Z^{\alpha}$) CO magnetization are stored separately and then subsequently added and subtracted, according to the IPAP procedure (Ottiger et al. 1998; Yang and Nagayama 1996). This produces a pair of data sets with peaks in the $^{13}CO$ dimension at frequencies of $\omega_{CO} \pm \pi J_{CO,C\alpha}$. Each of these data sets is shifted by $J_{CO,C\alpha}/2$ Hz (in opposite directions) so that peak positions correspond to chemical shifts, $\omega_{CO}$, and the two data sets added to increase the signal to noise further by $\sqrt{2}$. Note that the $N_Z \rightarrow H_Z$ pathway ($^{15}N$,$^{1}H^{N}$ spectrum) is unchanged by the IP/AP manipulations that are used for 'decoupling' of the $^{13}CO$ and $^{13}C^{\alpha}$ spins during $^{13}CO$ detection ($^{15}N$,$^{13}CO$ data) so that the IP and AP data sets can be added directly to increase the sensitivity of the $^{15}N$,$^{1}H^{N}$ correlation map by $\sqrt{2}$. As an aside, from Eq. 1 it is clear that the cosine-$t_1$ modulated $^{15}N$,$^{1}H^{N}$ data set is recorded at the same time as the sine-$t_1$ $^{15}N$,$^{13}CO$ spectrum so that the $^{15}N$ dimensions are 'reversed' in the two spectra.

Because the sensitivity of $^{13}C$ detect experiments is eightfold less than the corresponding $^{1}H$ observe measurements, all other things being equal, intensities of correlations in the $^{15}N$–$^{13}CO$ data set will be at least a factor of 8 reduced relative to the $^{15}N$–$^{1}H^{N}$ spectrum. The relative sensitivity difference is in fact larger because our cooled probe-head is optimized for $^{1}H$ and not $^{13}C$ detection, with the carbon coil further from the sample (signal to noise of 8050:1, $^{1}H$,ETB and 1030:1, $^{13}C$,ASTM). In addition, the pathway that generates the $^{15}N$–$^{13}CO$ spectrum is longer than that for the $^{15}N$–$^{1}H^{N}$ data set, since there is an additional element of duration $2\zeta$ where $^{13}CO$ magnetization is refocused with respect to the directly coupled $^{15}N$, that is longer than the final $2\tau_B$ and $2\tau_A$ delays that are required for the $^{15}N$–$^{1}H^{N}$ experiment. The 'starting magnetization' for each of the separate pathways can be controlled by the duration of $T_N$ since the sensitivities of the $^{15}N$–$^{1}H^{N}$ and $^{15}N$–$^{13}CO$ data sets are proportional to $\cos(2\pi J_{NCO}T_N)$ and $\sin(2\pi J_{NCO}T_N)$, respectively. Typically $T_N$ is chosen such that the cosine and sine terms are $\approx$0.174 and 0.985, respectively, although this could certainly be optimized on a case by case basis. It is noteworthy that the pulse scheme of Fig. 1 is constructed such that $t_{1,max}$ is not bounded by the value of $T_N$, so that the relative sensitivities of the $^{1}H^{N}$ and $^{13}CO$ detected data sets can be adjusted in a manner that does not depend on the required resolution in $F_1$. This is achieved by keeping the length of the scheme between points $a$ and $b$ constant for $t_1 \leq 2T_N$ and only increasing the length for $t_1 > 2T_N$ using a 'shared constant-time approach' (Grzesiek and Bax 1993; Logan et al. 1993). Of course, evolution of $^{15}N$ magnetization due to the one-bond $^{15}N$–$^{13}CO$ scalar coupling proceeds in all cases for a duration of $2T_N$.

Figures 2a, b illustrate 2D $^{15}N$–$^{1}H^{N}$ and $^{15}N$–$^{13}CO$ spectra of 1 mM, $^{15}N$,$^{13}C$ chicken liver fatty acid binding protein (Lb-FABP, 125 residues, 25 °C, 18.8T) recorded in approximately 20 min with the $^{15}N$,$^{1}H^{N}$‖$^{13}CO$ HSQC scheme of Fig. 1. Histograms of the signal-to-noise of cross-peaks in each of the spectra are shown in Figs. 2c, d. Although there is a significant sensitivity drop in the $^{13}CO$ detected spectrum the sensitivity is still more than sufficient to obtain a very near complete data set. In this regard it is of interest that 120 of the 122 expected peaks were observed in the $^{15}N$–$^{13}CO$ data set relative to 118 in the $^{15}N$–$^{1}H^{N}$ HSQC. The small difference is likely a reflection of slightly less overlap in the $^{15}N$–$^{13}CO$ spectrum.

The 2D $^{15}N$,$^{1}H^{N}$‖$^{13}CO$ HSQC experiment provides resonance frequencies of three nuclei, $^{13}CO$, $^{15}N$ and $^{1}H^{N}$, as in the 3D HNCO experiment (Ikura et al. 1990; Kay et al. 1990). Furthermore, not only do the two data sets, $^{15}N$,$^{1}H^{N}$ and $^{15}N$,$^{13}CO$ that are recorded in parallel, provide complementary information, but they also help to resolve ambiguities caused by signal overlap, because peak positions in the directly detected $^{1}H^{N}$ and $^{13}CO$ dimensions are typically not correlated, Fig. 2. Because the 2D spectra recorded here are the orthogonal $^{15}N$–$^{13}CO$ and $^{15}N$–$^{1}H^{N}$ projections of the 3D HNCO they can, in principle, be used together to reconstruct the 3D HNCO data set. In practice, it has been shown that while sparsely populated 3D spectra can be reconstructed by means of covariance processing (Kupce and Freeman 2007; Zhang and Bruschweiler 2004; Zhang et al. 2010) the signal overlap that is always present in 2D protein spectra causes many false correlations. These can be eliminated using projection spectroscopy (Freeman and Kupce 2004, 2012) or, as shown below, by recording the (missing) third orthogonal 2D plane, $^{13}CO$–$^{1}H^{N}$, using the HNCO pulse sequence. It then becomes possible to reconstruct the full 3D HNCO spectrum, at least for relatively small proteins. For example, extracting traces at a particular $F_3$ ($^{1}H^{N}$) frequency from the $F_1F_3$ ($^{13}CO$,$^{1}H^{N}$)

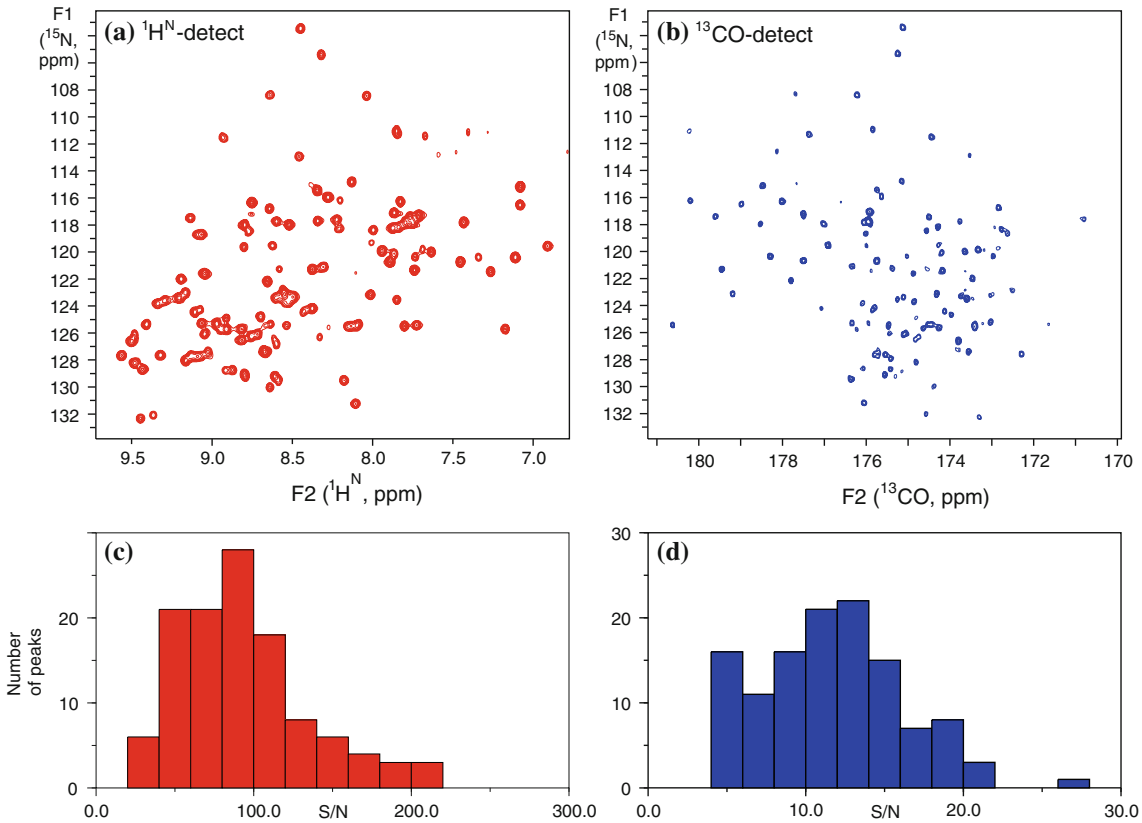


**Fig. 2** $^{1}H^{N}$ (**a**) and $^{13}CO$ (**b**) detected 2D HSQC spectra of the chicken liver fatty acid binding protein, 25 °C, (Lb-FABP, Asla Biotech, 1 mM in 9:1 $H_2O/D_2O$) recorded simultaneously using the pulse sequence of Fig. 1 on an Agilent 18.8T DDR2 NMR system equipped with two receivers and a cryogenic $^{13}C$ and $^{1}H$ enhanced sensitivity probe. The spectral widths were 2.8 kHz ($F_1$) and 12.5 kHz ($F_2$) with 128 ($t_1$) and 1,024 ($t_2$) complex data points. Data were collected in approximately 25 min using 2 scans per increment. Following acquisition, the IP and AP data sets were separated. These were added to increase the sensitivity of the $^{15}N,^{1}H^{N}$ correlation map by $\sqrt{2}$. For the $^{15}N,^{13}CO$ spectrum, the IP and AP data were added (data set A) and subtracted (data set B) in the time domain, each of the two data sets were frequency shifted by $\pm 0.5 J_{CO,C\alpha} = \pm 26$ Hz before adding together to increase the signal to noise further by $\sqrt{2}$. Histograms of signal-to-noise for the $^{15}N,^{1}H^{N}$ (**c**) and $^{15}N,^{13}CO$ (**d**) data sets are shown; 118 and 120 of the expected 122 correlations were quantified to produce the histograms in (**c**) and (**d**), respectively

and $F_2F_3$ ($^{15}N,^{1}H^{N}$) planes produces vectors, $\vec{v}_{F1-F3}$ and $\vec{v}_{F2-F3}$, whose tensor product $\vec{v}_{F1-F3} \otimes \vec{v}_{F2-F3}$ is the 2D $F_1F_2$ ($^{13}CO,^{15}N$) slice through the 3D data set at the $F_3$ frequency chosen. Unfortunately, many false peaks are produced using this procedure but these can be eliminated by retaining only those correlations present in an experimentally derived data set correlating $^{13}CO$ and $^{15}N$ chemical shifts, so long as such a plane is also available for analysis. The approach is illustrated in Fig. 3 using $^{13}CO$–$^{1}H^{N}$, $^{15}N$–$^{1}H^{N}$ and $^{15}N$–$^{13}CO$ planes recorded on Lb-FABP, the later two obtained using the HSQC scheme described above. A $^{13}CO$–$^{15}N$ 2D slice of the 3D HNCO data set at $F_3 = 7.11$ ppm is constructed from the tensor product of traces extracted at $\delta^{1}H^{N} = 7.11$ ppm from each of the $^{13}CO$–$^{1}H^{N}$, $^{15}N$–$^{1}H^{N}$ planes. These traces are shown in panels *a* and *b*, respectively, with the resulting tensor product indicated in panel *c*, red peaks. The false correlations are eliminated by comparison with the $^{15}N$–$^{13}CO$ plane, black in Fig. 3c, recorded using the sequence of Fig. 1. Only those peaks that are present in both the $\vec{v}_{F1-F3} \otimes \vec{v}_{F2-F3}$ and $^{15}N$–$^{13}CO$ planes are retained, to produce a high resolution data set that corresponds to a slice through the 3D HNCO spectrum, Figure d, red peaks. Figure d also overlays the corresponding slice obtained from an HNCO data set recorded conventionally and, not surprisingly, an excellent correlation in the peak positions between the two spectra is obtained. Notably, however, the resolution is vastly superior in the reconstructed slice, as illustrated in the traces in Figure d. This is emphasized further in Figure e where a slice corresponding to $F_3 = 8.80$ ppm is shown (both reconstructed and from a conventional data set), focusing on a more crowded region. As a final note it is straightforward to construct a high resolution, complete 3D HNCO spectrum by following a similar procedure to that described above for each $^{1}H^{N}$ frequency (Kupce and Freeman 2005).

The approach for recording the 2D $^{15}N,^{1}H^{N}\|^{13}CO$ HSQC experiment can be further expanded to generate 3D and

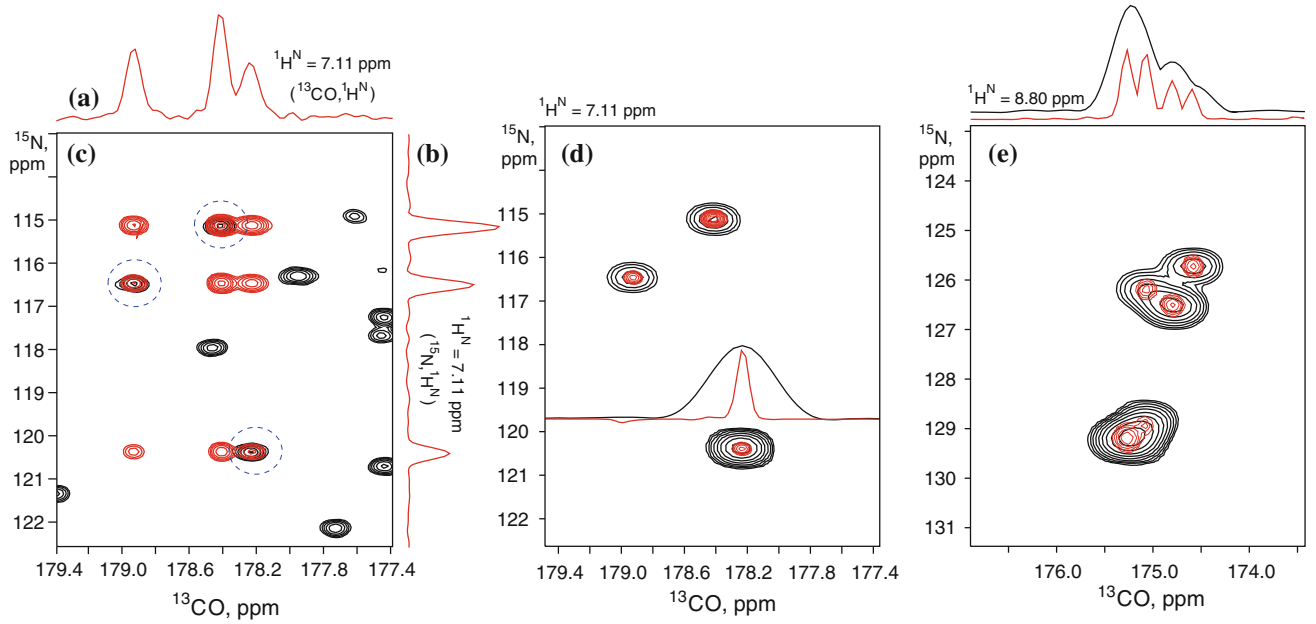


**Fig. 3** a, b Vectors corresponding to traces at $F_2 = 7.11$ ppm from high resolution 2D $^{13}CO$,$^1H^N$ and $^{15}N$,$^1H^N$ data sets (*red*) recorded on Lb-FABP, 25 °C, 18.8T. **c** As described in the text the tensor product of these vectors produces a 2D data set containing peaks found in the ($^{13}CO$,$^{15}N$) plane corresponding to the $F_3 = 7.11$ ppm slice from the 3D HNCO spectrum, along with many additional correlations (red). The 'real' peaks correspond to those that are found in the 2D $^{15}N$,$^{13}CO$ data set that is obtained from the sequence of Fig. 1 (*black*). Retaining only these peaks (overlap of *red* and *black* correlations, indicated by *circles*) generates the 'true' slice through the 3D but with much better resolution. Total measuring time to record all 3 orthogonal 2D planes was 35 min. **d** Fully reconstructed $^{15}N$,$^{13}CO$ plane (*red*) of the 3D HNCO ($F_3 = 7.11$ ppm) overlaid with the corresponding plane extracted from a 3D HNCO experiment recorded using the conventional HNCO pulse sequence in 6 h and 10 min with 32 ($t_1$), 64 ($t_2$) and 1,024 ($t_3$) complex data points and 2 scans per increment; 48 h would be required to record a conventional 3D spectrum with comparable resolution. **e** As in d but for $F_3 = 8.80$ ppm, showing a significant improvement in resolution in the case of overlapped peaks

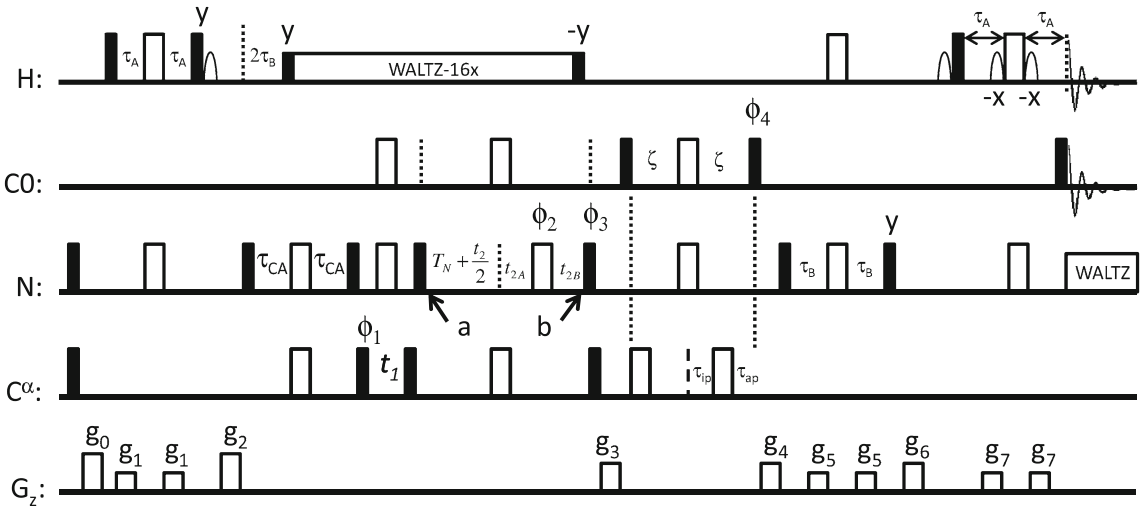


**Fig. 4** Pulse scheme of the 3D $^1H^N$||$^{13}CO$ HNCA. Many of the experimental details are the same as for the 2D $^{15}N$,$^1H^N$||$^{13}CO$ HSQC and are not repeated here (see legend to Fig. 1). The delay $\tau_{CA}$ is set to 14 ms. Phase cycling: $\phi_1 = x, -x$; $\phi_2 = 2(x), 2(y), 2(-x), 2(-y)$; rec (both $^1H$ and $^{13}CO$) = x, 2(−x), x. Quadrature detection in $F_1$ and $F_2$ was achieved by States-TPPI of $\phi_1$ and $\phi_3$ (set to y for the $\cos(\omega_N t_2)$ component of the $^1H^N$ detected data set), respectively (Marion et al. 1989); $\phi_4 =$ y, $\tau_{ip} = \zeta$ and $\tau_{ap} = 0$ to record the IP component and $\phi_4 = -$x, $\tau_{ip} = \zeta - \tau_{ap}$ and $\tau_{ap} = 4.86$ ms to record the anti-phase component. Gradient strengths (G/cm) and durations (ms): g0 = (10, 0.5), g1 = (5.0, 0.5), g2 = (15.0, 1.0), g3 = (10.0, 1.0), g4 = (7.0, 0.8), g5 = (−5.0, 0.3), g6 = (5.0, 0.6), g7 = (24.0, 0.5)

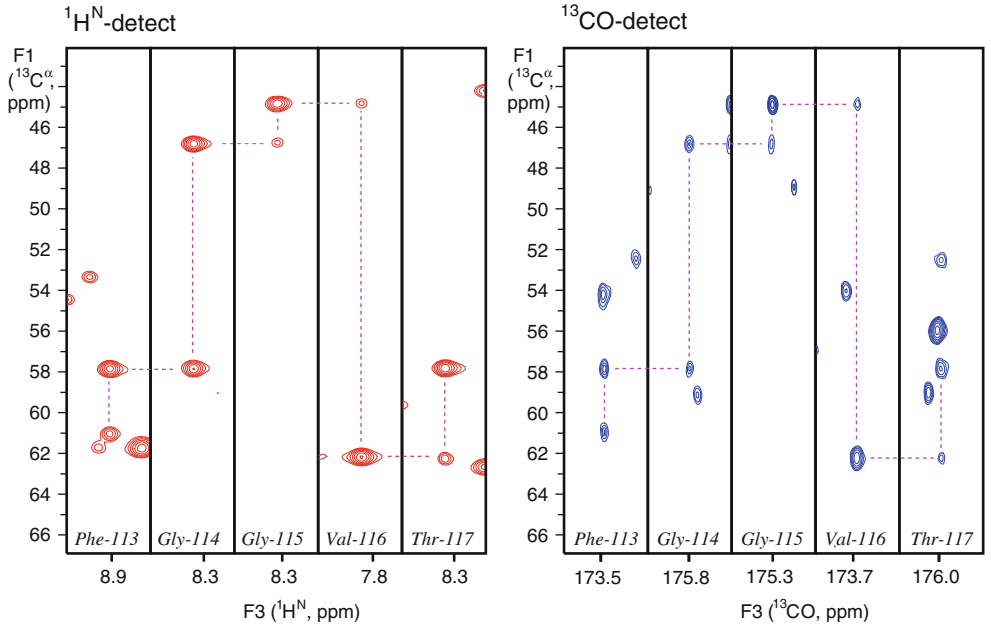


**Fig. 5** $F_1F_3$ strip plots of $^{1}$HN- (*left*) and $^{13}$CO- (*right*) detect 3D HNCA spectra of the chicken liver fatty acid binding protein (1 mM, 25 °C) recorded using the pulse scheme of Fig. 4 on an Agilent 18.8T DDR2 NMR system equipped with two receivers and a cryogenic $^{13}$C and $^{1}$H enhanced sensitivity probe. Spectral widths of 5 kHz ($F_1$), 2.8 kHz ($F_2$) and 12.5 kHz ($F_3$) were used, with 32 ($F_1$), 40 ($F_2$) and 1,024 ($F_3$) complex points. Following acquisition, IP and AP data sets were separated and the data sizes in the directly detected dimensions were reduced by a factor of 4 to retain only the active spectral bandwidths of interest. The data matrices were processed using linear prediction in the indirectly detected dimensions. The $^{13}$CO detected HNCA was generated by calculating sums and differences for the pairs of IPAP data sets, with a further $\sqrt{2}$ sensitivity advantage obtained by addition of the resulting spectra after frequency shifting the two data sets in $F_3$ by ±26 Hz. IP/AP data sets are added prior to processing the $^{1}H^{N}$-detected HNCA spectrum. The total experiment time was 11 h 20 min

higher dimensionality $^{1}H^{N}$- and $^{13}$CO-detected parallel experiments. We illustrate this via the 3D $^{1}H^{N}\|^{13}$CO HNCA, Fig. 4, and provide a brief description of the important features of the experiment below, neglecting pulse imperfections and relaxation. Similar to the 'traditional' HNCA pulse scheme (Ikura et al. 1990; Kay et al. 1990) magnetization is transferred according to the pathway

$$H_Z \rightarrow 2H_ZN_Z \rightarrow 2N_ZC_Z^{\alpha}\cos(\omega_{C\alpha}t_1) \qquad (2)$$

with $2N_ZC_Z^{\alpha}$ present immediately after the $t_1$ period. During the subsequent element, extending between points *a* and *b*, $^{15}$N magnetization is refocused with respect to $^{13}C^{\alpha}$, allowed to evolve (partially) due to the scalar coupling with the attached $^{13}$CO spin and chemical shift recorded (indirectly) so that immediately after gradient g3 the components of interest are proportional to

$$\sin(2\pi^{1}J_{NC\alpha}T_N)\cos(2\pi^{2}J_{NC\alpha}T_N)\{\cos(2\pi J_{NCO}T_N)\cos(\omega_N t_2)N_Z - \sin(2\pi J_{NCO}T_N)\sin(\omega_N t_2)2N_ZCO_Z\} \qquad (3)$$

There are additional terms to those in Eq. (3) that are also relevant, obtained by interchanging $^{1}J_{NC\alpha}$ and $^{2}J_{NC\alpha}$ above, however we will neglect these for simplicity. In the derivation of Eq. (3) it is noteworthy that we have included the fact that the $^{13}C^{\alpha}$ 90° pulse applied at point *b* purges any magnetization that has not refocused with respect to $^{13}C^{\alpha}$. This is important to obtain 'clean' IP and AP spectra for the $^{13}$CO detected pathway that follows. After point *b* the magnetization pathways for $^{1}H^{N}$ ($N_Z$) and $^{13}$CO ($2N_ZCO_Z$) detection diverge and the remaining portion of the sequence is identical to that already described for the $^{15}N,^{1}H^{N}\|^{13}$CO HSQC experiment, Fig. 1. Thus, a pair of 3D data sets are obtained with correlations at ($\omega_{C\alpha}$,$\omega_N$,$\omega_{HN}$) ($N_Z$ pathway)and ($\omega_{C\alpha}$,$\omega_N$,$\omega_{CO}$), with intensities proportional to $\sin(2\pi^{1}J_{NC\alpha}T_N)\cos(2\pi^{2}J_{NC\alpha}T_N)\cos(2\pi J_{NCO}T_N)$ and $\sin(2\pi^{1}J_{NC\alpha}T_N)\cos(2\pi^{2}J_{NC\alpha}T_N)\sin(2\pi J_{NCO}T_N)$, respectively. For $T_N = 0.014$ and for small to moderately sized proteins the signal is close to optimal for the $^{13}$CO HNCA, with sufficient signal for the second pathway so that high quality $^{1}H^{N}$ HNCA data sets can be obtained.

A 3D $^{1}H^{N}\|^{13}$CO HNCA data set has been recorded on a 1 mM $^{15}N,^{13}$C labelled Lb-FABP sample, 18.8T, 25 °C in 12 h of acquisition time. Figure 5 compares strip plots from the pair of 3D data sets. High quality data sets are obtained, with 119 intra- and inter-residue correlations and 116 intra-, 109 inter-residue cross-peaks observed in the $^{1}H^{N}$ and $^{13}$CO detect experiments, respectively (out of a possible 122). A comparison of both data sets makes it very easy to link $^{1}H^{N}$ and $^{13}$CO chemical shifts and because the

$^{13}$CO chemical shift is recorded directly much higher resolution can be obtained than from 'standard' HNCO data sets. This is illustrated in Figs. 3d,e where significant differences between $^{13}$CO line-widths in directly/indirectly detected dimensions are noted.

In summary we have shown that $^{1}H^{N}$ and $^{13}$CO detected 2D and 3D experiments can be recorded simultaneously and with high resolution. Such experiments provide more information in a single measurement in comparison to conventional experiments recorded with a single receiver. For instance, the backbone assignment of small to medium size proteins ($^{1}H^{N}$,$^{15}$N,$^{13}C^{\alpha}$,$^{13}$CO) can potentially be obtained from a single pulse sequence that uses parallel acquisition, such as 3D $^{1}H^{N}$||$^{13}$CO HNCA (except for prolines). With the prospect of further increases in the sensitivity of $^{13}$C detection we expect such experiments to become routine in the near future.

**Acknowledgments** This work was supported by a grant from the Natural Sciences and Engineering Research Council of Canada to L.E.K. L.E.K. holds a Canada Research Chair in Biochemistry.

## References

Bax A (1994) Multidimensional nuclear magnetic resonance methods for protein studies. Curr Opin Struct Biol 4:738–744

Chakraborty S, Paul S, Hosur RV (2012) Simultaneous acquisition of 13Calpha-15 N and 1H–15 N–15 N sequential correlations in proteins: application of dual receivers in 3D HNN. J Biomol NMR 52:5–10

Clore GM, Gronenborn AM (1991) Structures of larger proteins in solution: three- and four-dimensional heteronuclear NMR spectroscopy. Science 252:1390–1399

Freeman R, Kupce E (2004) Distant echoes of the accordion: reduced dimensionality, GFT NMR, and projection-reconstruction of multidimensional spectra. Concepts in Magn. Reson. 23A:63–75

Freeman R, Kupce E (2012) Concepts in projection-reconstruction. Top Curr Chem 316:1–20

Grzesiek S, Bax A (1993) Amino acid type determination in the sequential assignment procedure of uniformly 13C/15 N-enriched proteins. J Biomol NMR 3:185–204

Ikura M, Kay LE, Bax A (1990) A novel approach for sequential assignment of 1H, 13C, and 15 N spectra of proteins: heteronuclear triple-resonance three-dimensional NMR spectroscopy. Application to calmodulin. Biochemistry 29:4659–4667

Kay LE, Ikura M, Tschudin R, Bax A (1990) Three-dimensional triple-resonance NMR spectroscopy of isotopically enriched proteins. J Magn Reson 89:496–514

Kupce E (2011) NMR with multiple receivers. Top Curr Chem. doi: 10.1007/1128_2011_1226

Kupce E, Freeman R (1996) Optimized adiabatic pulses for wideband spin inversion. J Magn Reson Ser A 118:299–303

Kupce E, Freeman R (2005) Fast multi-dimensional NMR: radial sampling of evoluiton space. J Magn Reson 173:317–321

Kupce E, Freeman R (2007) Natural-abundance 15 N–13C correlation spectra of vitamin B-12. Magn Reson Chem 45:103–105

Kupce E, Freeman R (2008) Molecular structure from a single NMR experiment. J Am Chem Soc 130:10788–10792

Kupce E, Freeman R (2011) Parallel receivers and sparse sampling in multidimensional NMR. J Magn Reson 213:1–13

Kupce E, Freeman R, John BK (2006) Parallel acquisition of two-dimensional NMR spectra of several nuclear species. J Am Chem Soc 128:9606–9607

Kupce E, Kay LE, Freeman R (2010) Detecting the "afterglow" of 13C NMR in proteins using multiple receivers. J Am Chem Soc 132:18008–18011

Logan TM, Olejniczak ET, Xu RX, Fesik SW (1993) A general method for assigning NMR spectra of denatured proteins using 3D HC(CO)NH-TOCSY triple resonance experiments. J Biomol NMR 3:225–231

Marion D, Ikura M, Tschudin R, Bax A (1989) Rapid recording of 2D NMR spectra without phase cycling. Application to the study of hydrogen exchange in proteins. J Magn Reson 85:393–399

Ottiger M, Delaglio F, Bax A (1998) Measurement of J and dipolar couplings from simplified two-dimensional NMR spectra. J Magn Reson 131:373–378

Wüthrich K (1986) NMR of proteins and nucleic acids. Wiley, New York

Yang D, Nagayama K (1996) A sensitivity-enhanced method for measuring heternuclear long-range coupling constants from the displacement of signals in two 1D subspectra. J Magn Reson Ser A 118:117–121

Yang D, Venters RA, Mueller GA, Choy WY, Kay LE (1999) Trosy-based HNCO pulse sequences for the measurement of 1HN–15 N, 15 N–13CO, 1HN–13CO, 13CO–13Ca dipolar couplings in 15 N, 13C, 2H-labeled proteins. J Biomol NMR 14:333–343

Zhang F, Bruschweiler R (2004) Indirect covariance NMR spectroscopy. J Am Chem Soc 126:13180–13181

Zhang F, Bruschweiler-Li L, Bruschweiler R (2010) Simultaneous de novo identification of molecules in chemical mixtures by doubly indirect covariance NMR spectroscopy. J Am Chem Soc 132:16922–16927